Multiwalled Carbon Nanotube Photonic Crystals for Extreme-UV Photonics based on Comprehensive Dielectric Function Modeling

Yasser Shamsollahi[iD], Mohammad Kazem Moravvej-Farshi[iD]

Faculty of Electrical and Computer Engineering, Tarbiat Modares University, Tehran, Iran

ABSTRACT: Our latest study builds upon our previous research on multi-wall carbon nanotubes (MWCNTs) by exploring the photonic responses of regularly β-aligned arrays of these nanotubes. Through extensive calculations using the Finite Difference Time Domain Method, we determined that MWCNT-based photonic crystals possess significant Bragg reflections of up to 80% without experiencing substantial attenuation, even at wavelengths as low as 17 nm. This discovery is of great significance, as traditional materials have not been able to scatter UV photons within this frequency range efficiently. Following extensive research, we analyzed various model parameters such as lattice periodicity, inner and outer radii of MWCNTs, and the polarization (TM or TE) and direction (Γ-X or Γ-M) of the incident wave. Our findings present promising implications for advancing ultra-high-frequency photon manipulation in EUV applications, with potential developments ranging from UV laser mirrors to EUV lithography lenses, and beyond to UV spectroscopy collimators.

1- Introduction

Carbon nanotubes (CNTs) are unique materials that exhibit strong anisotropy [1-3] and high nonlinearity [4, 5], making them ideal for various optical applications, such as infrared (IR) detectors, photoluminescence [6], and as scatterers for photonic crystals [7-10]. Recent advancements have enabled precise control over the growth of multi-wall CNTs (MWCNTs) arrays [11-13], which exhibit Bragg scattering behavior across an ultra-wide frequency range (visible to deep ultraviolet (UV)) [8, 10]. Unlike in single-wall CNTs, the chirality of MWCNT shells does not influence their optical properties [10, 14], and their dielectric responses closely resemble those of anisotropic graphite [2, 3]. Therefore, modeling MWCNT dielectric responses using the dielectric functions of graphite ($\varepsilon_\parallel(\omega)$ and $\varepsilon_\perp(\omega)$) is possible. The symbol $\perp(\parallel)$ denotes the direction perpendicular (parallel) to the graphite optical (c) axis or radial of a MWCNT. Hence, the $\perp$ direction is equivalent to the z or ϕ-axis of an MWCNT, and $\varepsilon_\perp(\omega) \equiv \varepsilon_{TM}(\omega)$ corresponds to the MWCNT's dielectric response to a TM polarized signal. In contrast, the dielectric response to a TE polarized signal is a complex function of $\varepsilon_\parallel(\omega)$ and $\varepsilon_\perp(\omega)$ in graphite. The lattice constant (a) and arrangement of an MWCNT-based PhC, the MWCNT's inner and outer radii, their permittivities in response to both TE and TM incident waves, and the direction of the incident signal

propagation play significant roles in determining the optical properties of the MWCNT-PhCs. Although some reports have touched upon the experimental and theoretical aspects of MWCNT-PhCs, most have focused on frequencies from visible up to the UV range [7-10, 15, 16]. Nonetheless, recent theoretical and experimental works suggest that CNTs hold promise in overcoming the technological limitations of deep and extreme UV frequencies [1, 7, 9, 17].

The dielectric function of graphite ($\varepsilon_\perp(\omega)$) fitted with the Drude-Lorentz (DL) formula is applied to simulate the optical response to a TM polarized signal using the finite difference time domain method (FDTD). On the other hand, in response to a TE-polarized signal, one should use a model for $\varepsilon_{TE}(\omega)$ describing the dielectric function of an individual MWCNT. However, available models used up to now are either an oversimplified model —i.e., $\varepsilon_{TE}(\omega) \equiv (\varepsilon_\perp(\omega) \cdot \varepsilon_\parallel(\omega))^{1/2}$ [18] — or that of an effective medium for α-aligned MWCNTs on a dielectric, extracted by a self-consistent method [19]. In this paper, we use an analytic function that we developed earlier [10] for $\varepsilon_{TE}(\omega)$ of an individual MWCNT based on a discreet dipole approximation framework for cylindrical fullerenes [20]. To obtain that analytic function for $\varepsilon_{TE}(\omega)$, unlike the other theoretical studies, we took the anisotropic nature of the MWCNT cylinders into account, constructing it based on susceptibility well-fitted to experimental and semi-empirical data down to wavelengths ~30 nm. In this work, we extrapolated that model via inductive reasoning down to

*Corresponding author's email: moravvej@modares.ac.ir

~17 nm, where the material response is approaching zero. The extrapolated model has enabled us to study the photonic properties of the designed MWCNT-PhC platforms over a broader frequency range.

The development of spectroscopic techniques using deep UV light with wavelengths below 300 nm faces significant challenges due to the limited availability of optical components designed for this spectral range. The absorption characteristics of many materials in the UV spectral range often impede their performance in deep UV optics [21].

To the best of our knowledge, up to date, the commonly used devices in the visible and near-infrared spectral ranges to select specific bandwidth spectral regions for detection and wide-field manipulating and imaging have not been demonstrated for the deep to extreme UV spectral regions.

We have recently developed deep to UV diffracting PhCs that could serve as up to UV photonic devices [10]. In that work, we have modeled the dielectric function of MWCNTs based on the fundamental polarizability formula. Here, we show that further advancements in extreme UV diffracting PhCs could lead to their commercialization as Rayleigh rejection optics, optical EUV filters, wide-field imaging optics, and dielectric or dichroic mirrors, EUV waveguides, and lenses designed to reflect, guide, and collimate specific wavelengths.

However, a current challenge in developing PhCs for extreme UV spectroscopic instrumentation lies in the top-down fabrication techniques, which pose pattern-perfectness inabilities. On the other hand, MWCNT arrays utilize bottom-up approaches, showing orderly erected arrays of nanotubes composed of ultra-high aspect ratios (diameter to height ratio = d/l).

Recall that most material bandgaps are smaller than the energy of extreme ultraviolet (EUV) photon of $\lambda < 200$ nms, exhibiting a notable absorption characteristic [22]. Although a periodic arrangement of quarter-wavelength slabs of two different materials with a sufficient refractive index contrast could result in an excellent Bragg reflector [23], due to the intricate nature of the refractive index of materials, approaching unity at shorter wavelengths [24], the refractive index contrast of the two quarter-wavelength slabs at EUV becomes insignificant diminishing the required Bragg reflectance. For this reason, there is currently a lack of firmly established pairs of nanoscale slabs, particularly at $\lambda < 40$ nm, capable of achieving the requisite reflectance levels for numerous applications involving soft X-ray optics, such as astronomy, X-ray lasers, plasma diagnostics, and spectroscopy [25-27].

Typically, the wavelength of a photonic bandgap (PBG) closely aligns with the periodicity of the crystal. If one employs MWCNTs as scatterers in photonic crystals, their lattice constants spanning tens to hundreds of nanometers, the resulting PBG could fall within the EUV wavelength range of 15 to 300 nm.

In this study, we designed vertically (β)-aligned multi-walled carbon nanotube arrays to serve as 2D EUV photonic crystal structures, and we conducted both physical modeling

and theoretical simulation and investigations into its reflectance properties in the extreme ultraviolet spectrum. The photonic properties of the arrays mentioned before at EUV wavelengths could be assessed utilizing synchrotron radiation [28]. Here, we extrapolate our earlier model [10] via inductive reasoning down to 17 nm (the EUV range), where the material response is approaching zero The extrapolated model has enabled us to study the photonic properties of the designed MWCNT-PhC platforms over a broader frequency range.

2- Formulation

When the MWCNT length (l), is much longer than the incident light wavelength (λ) and at the same time much larger than the CNT diameter (d), one may use a 2D analysis to describe the photonic response of the MWCNT-PhC. Today, MWCNT arrays can be produced to satisfy both conditions for terahertz frequencies and higher [11-13]. For a detailed description and validation of the physical permittivity model, refer to the Appendix.

The dispersive dielectric function of a cylindrical MWCNT can be described by a tensor [20]:

$$\bar{\bar{\varepsilon}}(\omega) \equiv \bar{\bar{\varepsilon}}_{\parallel}(\omega) + \bar{\bar{\varepsilon}}_{\perp}(\omega) \equiv \varepsilon_{\parallel}(\omega) R\boldsymbol{\rho} + \varepsilon_{\perp}(\omega)(\Phi\boldsymbol{\phi} + Z\mathbf{z}) \quad (1)$$

where $\boldsymbol{\rho}$, $\boldsymbol{\phi}$, and $\mathbf{z}$ are unit vectors of cylindrical coordinates.

Recall that $\varepsilon_{TM}(\omega) \equiv \varepsilon_{\perp}(\omega)$. Lower and upper Triangles in Fig. 1(a) denote the experimentally measured data for real (Re) and imaginary (Im) parts of $\varepsilon_{TM}(\omega)$ that satisfy the Kramers-Kronig (KK) transformation and are tabulated in [29]. The dotted line and dashes represent the fit to the DL model provided by [8]. On the other hand, $\varepsilon_{TE}(\omega)$ that comprises both $\varepsilon_{\perp}$ and $\varepsilon_{\parallel}$ of graphite can be modeled (See Appendix):

$$A\varepsilon_{TE}^2 + B\varepsilon_{TE} + C = 0 \quad (2)$$

To obtain the constants *A*, *B*, and *C* as given by (A.3.b)-(A.3.d), in addition to the data mentioned above for $\varepsilon_{\perp}$, collective experimental data for $\varepsilon_{\parallel}$ presented by [30] were also utilized. Setting *m*=1 and ρ=0.2 as a typical ratio in (A.3.b) to (A.3.d), one can obtain $\varepsilon_{TE}(\omega)$ by solving (2). The lower and upper Triangles in Fig. 1(b) depict the real and imaginary parts of $\varepsilon_{TE}(\omega)$ calculated in this manner [10]. The dotted line and dashes show the fit to the DL model of (A.4) using the fit parameters tabulated in Table A.1 [31].

As the optical response of any material converges to unity at ultra-high frequencies, based on the associated Drude-Lorentz (DL) model, it is reasonable to anticipate that the permittivity function be seamlessly extrapolated via inductive reasoning. This extrapolation occurs smoothly beyond the
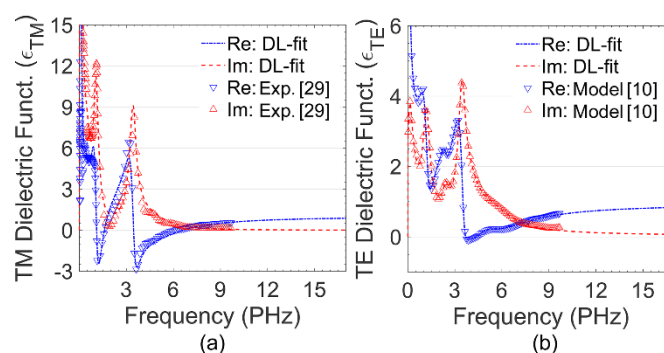
Fig. 1. Kramers-Kronig constraint Drude-Lorentz dielectric function of an individual MWCNT to (a) TM [29] and (b) TE [10] incident waves.

frequency of 5 PHz (Figure 1) and exhibits no additional fluctuations. Consequently, we extend the DL models until the response converges to their infinity response, which transpires at approximately 17.5 PHz, corresponding to an energy level of ~ 71.5 eV ($\lambda \sim 17$ nm).

3- Results and Discussions

Figure 2 illustrates schematics of the top views of two 2D-PhCs, each made of a 2D array of MWCNTs of inner and outer radii of r and R, with a square lattice of pitch 'a' oriented along (a) Γ-X and (b) Γ-M direction. On the right side of each lattice, a square of side 'a' represents the affiliated unit cell, wherein the triangle ΓXM describes the corresponding irreducible Brillouin zone. The two coordinate systems depicting the polarization directions of TM and TE incident waves are also shown on the right. We took the number of MWCNT columns along the propagation direction (x) to be N and infinite along the y-direction, utilizing the periodic boundary conditions (PBC). The optical power threshold for the nonlinear effects in CNTs can vary depending on their specific types and experimental conditions. Generally, it ranges from a few hundred W/m^2 to several KW/m^2. Since the nonlinear effects are not a concern of the present study, we assume a low input power of 1 W/m^2, as in similar studies [8, 10].

Thanks to the availability of physical and corresponding DL models for dispersion relations of individual MWCNTs for both TM and TE incident waves, we can now accurately predict the photonic responses of the MWCNT-PhC depicted in Figure 2 for both polarizations. Generally, the photonic response of a PhC is contingent upon its lattice type, geometrical parameters (such as a, r, R, and N), and the polarization and direction of the incident wave relative to the PhC's lattice line of symmetry (Γ-X or Γ-M). The following subsections explore how these parameters influence the PhC's optical responses (from UV to EUV).

Fabricating periodic arrays of MWCNTs with a maximum periodicity of a few tens of nanometers for applications in UV and EUV devices requires advanced techniques such as electron beam lithography (EBL) combined with a templating process, nanoimprint lithography, and interference lithography, by either of which one can grow the desired arrays nanotubes on integrable substrates such as Si and sapphire. An example is using EBLE to pattern a resist layer and then templating the pattern onto the substrate to create periodic arrays of MWCNTs [32]. An alternative method is nanoimprint lithography, a high-throughput, high-resolution patterning technique that enables one to create periodic arrays of MWCNTs by transferring a pattern from a mold to a substrate [33]. The third technique is interference lithography, which involves using the interference pattern of multiple coherent light beams to create periodic nanostructures. This technique can enable the fabrication of large-area periodic arrays of MWCNTs with precise control over the periodicity [34].

3- 1- Dependency of the Bragg response on the polarization and lattice orientation

We examined two PhC arrays as depicted in Figure 2, having identical parameters ($N = 200$, $a = 25$ nm, $R = 5$ nm, and $r = 1$ nm). Each PhC was subjected to an incident wave of either TM (TE), which struck it along its line of symmetry Γ-X (Γ-M). Analyzing the optical responses of the PhCs, we calculated the reflectance spectra for all four scenarios (Fig. 3). The diagram illustrates two pairs of reflectance peaks occurring at ~1.1 and ~ 3.4 PHz for the TM: Γ-X and TM: Γ-M (see the inset) which predominantly stem from metallic-like characteristics (i.e., non-Bragg reflections) [10]. Notably, the frequencies of these two peaks correspond to the frequencies at which the two minima in the $Re(\varepsilon_{TM})$ appear, as depicted by the blue dotted line in Figure 1(a). These minima result from internal excitations within the graphite layers associated with
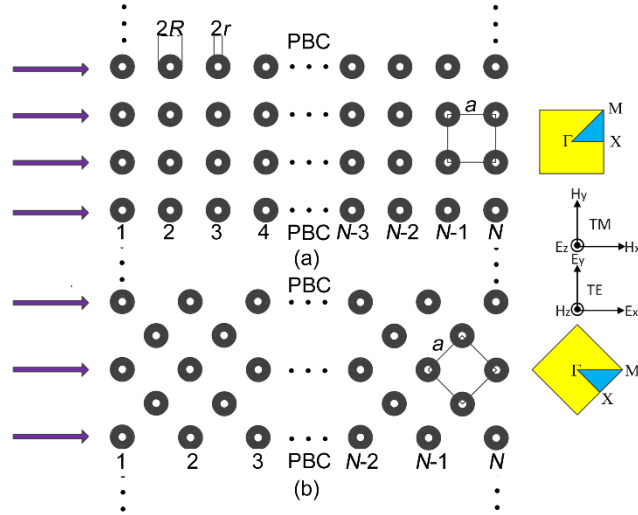
Fig. 2. Schematics of the top views of a square lattice 2D-PhC of constant a, oriented along (a) Γ-X and (b) Γ-M. The yellow squares on the right represent the Brillouin zones in which cyan triangles represent irreducible Brillouin zones. Areas surrounded by the solid lines represent the corresponding unit cells.
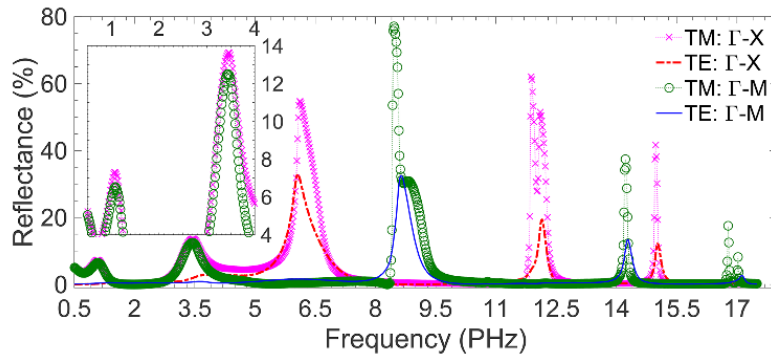
Fig. 3. Reflectance spectra for given values of N =200, a =25 nm, R = 5 nm, and r = 1 nm, in response to combinations of polarization and lattice orientation of TM:Γ-X, TE:Γ-X, TM:Γ-M, and TE:Γ-M. The inset depicts a zoomed-in portion of the spectra for better distinction of the material-dependent (non-Bragg) peaks for TM: Γ-X and TM; Γ-M.

π and σ bonds [35].

When a TE incident wave is applied to this PhC, the metallic-like resonances it generates are minimal. This is due to the effective inter-atomic distance, which is perceived by an in-plane electric field and equals the inter-layer spacing. In contrast, the actual inter-atomic distance along the axis of the CNT, which is experienced by a TM incident wave is 2.7 times smaller than the inter-layer spacing. To simplify, the number of excited electrons contributing to the resonances sensed by a TE incident wave is significantly lower than those a TM incident wave can excite along the MWCNT

axes. This is because the in-plane component of the electric field vector within the graphitic plane primarily excites hybrid sp^2 covalent bonds. Equation (2) demonstrates this limitation, presenting the model for $\varepsilon_{TE}(\omega)$. Essentially, for the TE incident, the motion of free carriers is confined within each MWCNT shell. In contrast, for the TM incident, carriers' movement can extend over the entire length (l) of the MWCNT.

The graph in Fig. 3 shows some additional peaks that are visible in the frequency range above 5 PHz. These peaks are influenced by factors such as the polarization of the incident

wave, and the lattice type and geometry, and describe respective Bragg's reflections. The real and imaginary components of both ε_{TM} and ε_{TE} have insignificant frequency dependence in this range (as seen in Fig. 1). The strength of reflectance in each case depends on the effective refractive index contrast sensed by the corresponding polarization and the attenuation in the related frequency range. In other words, similar to what is observed in conventional pillar-based PhCs, the difference between each TE reflectance peak and its TM counterpart, like the difference in their corresponding photonic bandgaps, is due to the difference between the refractive index contrasts effectively sensed by the TE and TM incident waves.

According to the data presented in Figure A.1 (i.e., $\text{Re}(n_{TM}) < \text{Re}(n_{TE}) < 1$), the Bragg effect is more pronounced for the TM incident wave compared to the TE counterpart, in both lattice orientations. On the other hand, one can see that the first Bragg response for TM:Γ-X around 6 PHz starts before the second metallic-like response around 3.4 PHz entirely vanishes. The constructive interference between them, results in higher metallic-like reflections for TM:Γ-X compared to TM:Γ-M, despite both having identical parameters and fill factor (ff). Furthermore, Figure 3 indicates that the TM incident wave exhibits high reflectance for frequencies below 0.5 PHz, which is attributed to the Drude dispersive nature of MWCNTs [36].

3- 2- Dependency of Bragg's Response on N

For a Bragg resonance to build in a photonic crystal based on MWCNTs (MWCNT-PhC), we require a sufficient number of MWCNT columns (*N*) along the propagation direction. However, due to inherent MWCNT loss, the maximum Bragg reflectance from an MWCNT-PhC will always be less than 100%. As we increase the number of columns (*N*), the Bragg reflectance will reach its maximum value. Beyond this point, any further increase in *N* would only cause a gradual decrease in the saturated reflectance spectra. Therefore, this sub-section focuses on determining the ideal value of *N* for each given condition under study to optimize the fabrication cost. The analysis presented in this study provides valuable insights into the design and optimization of MWCNT-PhCs for various applications in photonics and optoelectronics.

Here, keeping all parameters fixed as mentioned in sub-section 3.1 and varying (*N* = 50, 100, 200, and 400), we calculated the reflectance spectra for both lattice orientations of Fig. 2 when illuminated by both TE and TM incident waves. Figure 4 illustrates the numerical results in separated spectral windows for each case to make each spectrum as distinct as possible. Figures 4(a) and 4(b) show Bragg reflection spectra of the square lattice PhCs in response to TM and TE incident waves when lined up with Γ-X direction. Figures 4(c) and 4(d) depict similar spectra for the square lattice when the TM and TE incident waves lined up with Γ-M.

After a thorough analysis of Figure 4, it is crystal clear that the reflectance spectra peaks at the Bragg resonance frequencies depict two consistent patterns across all four cases, except for the lower frequencies of the Γ-M orientation

when *N* increases. Firstly, the peaks unquestionably rise, as expected. Secondly, it is evident that once *N* exceeds the value of 200, the increase in the peaks becomes trivial. This phenomenon strongly suggests that 200 is indisputably the optimal number of MWCNT columns along the propagation direction (*x*) for both Γ-X and Γ-M orientations. At around 8.5 (8.6) PHz, the Bragg reflectance peak of a TM (TE) polarized input signal from the Γ-M orientation begins to decrease when the number of MWCNT columns surpasses 50. This occurrence can be explained by the rise in metallic loss of the MWCNTs, which stems from the imaginary components of the effective dielectric constants of the MWCNT arrays matched with the polarization ($\text{Im}\varepsilon_{TM}(\omega)$ and $\text{Im}\varepsilon_{TE}(\omega)$) at the corresponding Bragg resonance frequency of the Γ-M orientation (see Fig. 4 of [8]).

3- 3- Effect of lattice constant on photonic responses

In this part, we examined how altering the lattice constant (*a*) affects the optical responses of MWCNT-PhCs, as depicted in Fig. 2. Our simulations involved testing both TM and TE polarized input signals with fixed $N = 200$ and ratios of $R/a = 0.2$ and $\rho = r/R = 0.2$ [10] while varying *a* between $10 \leq a \leq 80$ nm. The reflectance spectra from the different PhC structures were analyzed for Γ-M and Γ-X orientations, as shown in Fig. 5.

Our findings indicate that when the lattice constant is reduced to 10 nm, only one Bragg resonance frequency falls within the frequency range under investigation for Γ-X orientation at 15.03 (15.05) THz for TM (TE) polarized signal. However, no Bragg resonance occurs for Γ-M orientation in the shown frequency range. On the other hand, for $a = 20$ nm, first harmonics Bragg resonances for all four cases are observed around ~7.6 and ~10.7 PHz for Γ-X and Γ-M orientations, respectively, and either polarization. As the lattice constant increases, the first harmonic of the Bragg response exhibits a significant redshift for each case shown. This redshift is so significant that the first TM Bragg resonance for $a \geq 40$ tends to overlap the corresponding second metallic-like resonance, gradually leaving it behind and approaching the first metallic-like resonance for $a \geq 80$ nm.

An unexpected observation has been made in the photonic response of TM:Γ-X for $a = 80$ nm. Specifically, a dip in the first harmonic of the Bragg resonance has been observed between 3 to 4 PHz, where the material response is expected to appear. This dip is attributed to the incoherent addition of the Bragg and metallic responses, resulting in their mutual cancellation.

### 3- 4- Effect of R (R/a) on photonic responses

The photonic response of MWCNT-PhC is significantly influenced by the size of the MWCNTs' outer radii (*R*). To investigate this parameter dependency, we maintained values of *a*=25, $\rho = r/R = 0.2$, and *N*=200 constant and varied the value of *R*. The Bragg reflectance spectra for MWCNT-PhC under TM and TE polarized input signals, oriented in the Γ-X direction, are illustrated in Figs. 6(a) and 6(b), respectively. Similarly, Figures 6(c) and 6(d) depict similar spectra for TM
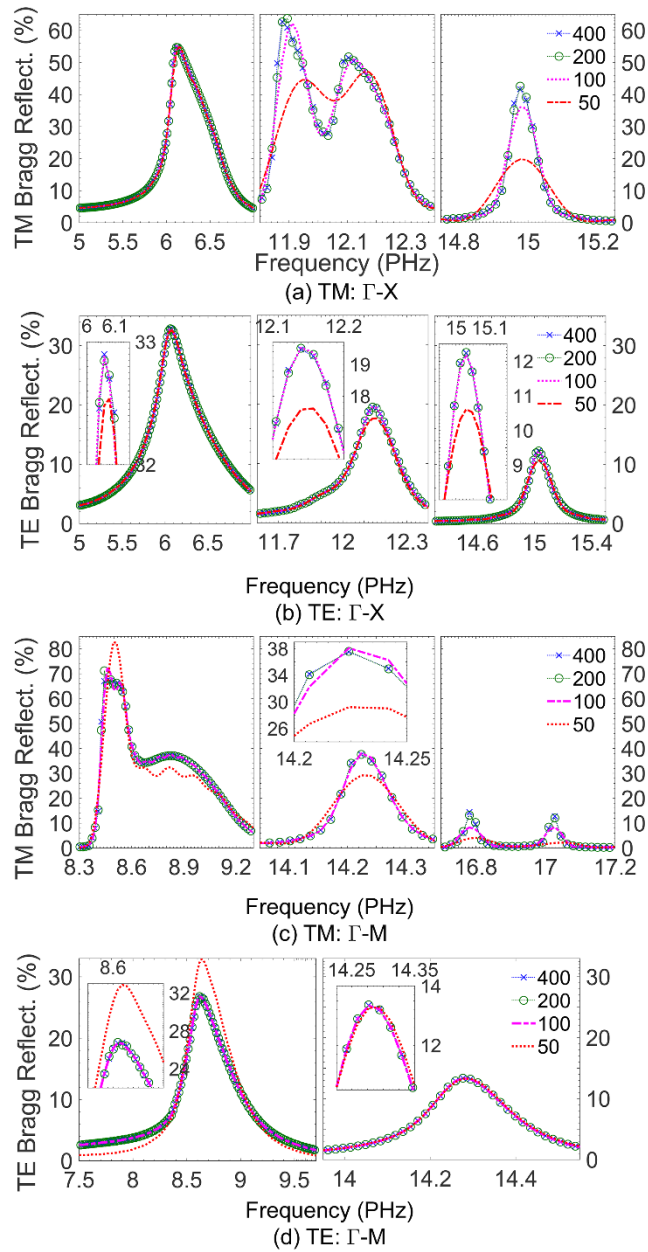
Fig. 4. The Bragg reflectance spectra for different numbers of rows and given values of a =25 nm, R = 5 nm, and r = 1 nm, in response to combinations of polarization and lattice orientation (a) TM:Γ-X, (b) TE:Γ-X, (c) TM:Γ-M, and (d) TE:Γ-M. Insets show how close some peaks are to each other.
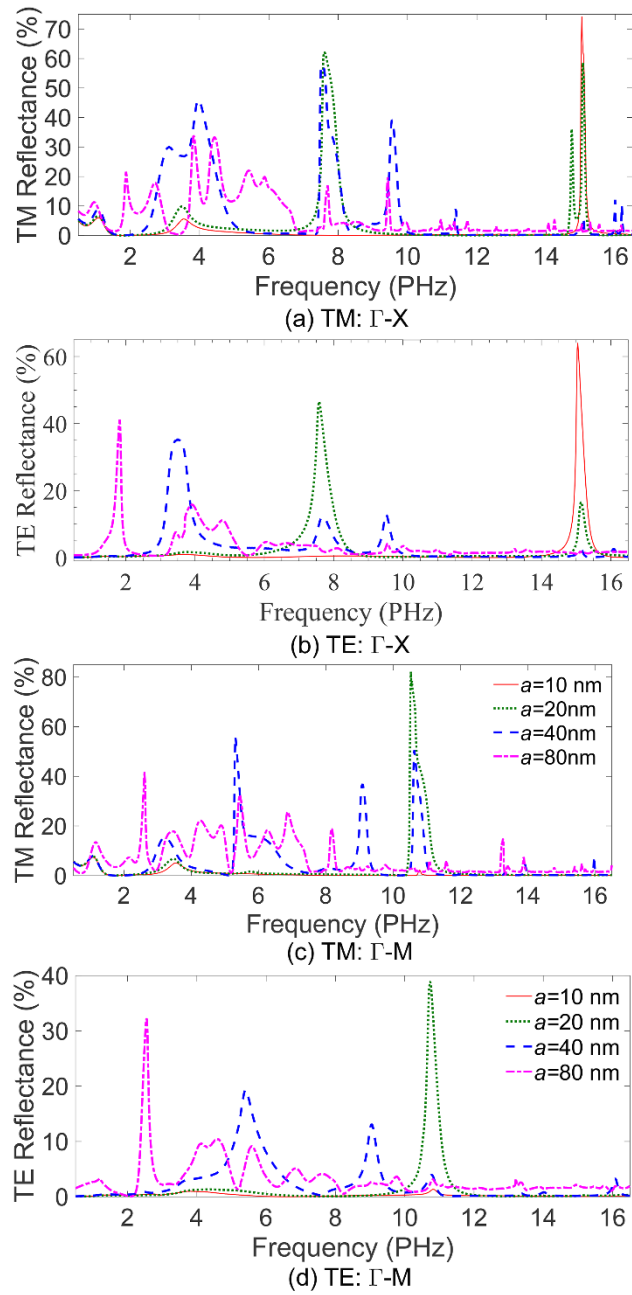
Fig. 5. Reflectance spectra for various lattice constants and given values of N = 200, r = 1 nm, and R / a = 0.2, in response to combinations of polarization and lattice orientation (a) TM:Γ-X, (b) TE:Γ-X, (c) TM:Γ-M, and (d) TE:Γ-M.
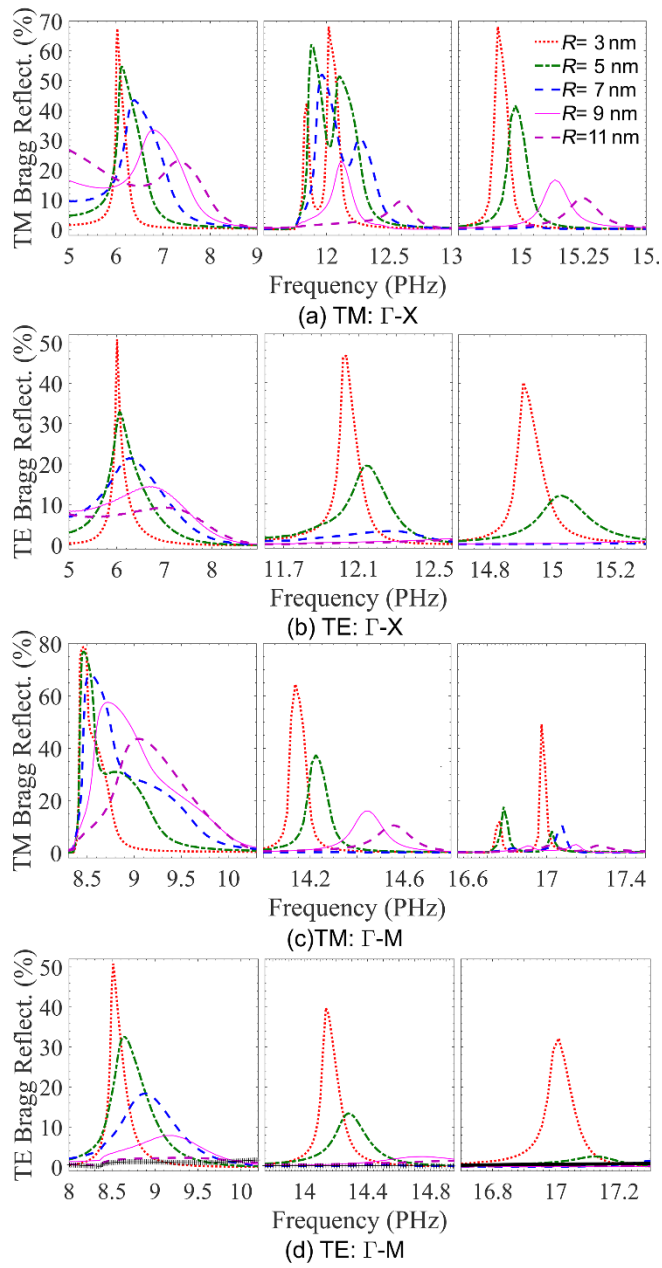
Fig. 6. Bragg reflectance spectra for various R and given values of N = 200, a =25 nm, and R/a =r/R = 0.2, in response to combinations of polarization and lattice orientation (a) TM:Γ-X, (b) TE:Γ-X, (c) TM:Γ-M, and (d) TE:Γ-M.

Table 1. Comparison of the present work and previously published studies on MWCNT-PhCs

REFERENCE	STUDY TYPE	FREQUENCY RANGE	POLARIZATION	PHYS. MODEL FOR THE DIELECTRIC FUNCTION	MWCNT HOLLOW CORE EFFECT	DRUDE-LORENTZ MODEL FOR WIDE-RANGE SIMULATION	K-K COMPATIBLE	R (%)
[7]	E	Visible	TM	–	–	–	–	N/A
[8]	T	UV to EUV (≤ 10 PHz)	TM	No	No	Yes	No	68%
[9]	E/T	Vis-IR	TM	–	–	–	–	N/A
[10]	T	Deep UV	TM/TE	Yes	Yes	Yes	Yes	75%
[15]	T	Vis-IR	TM	No*	No	No	No	N/A
[16]	E/T	IR	TM/TE	No*	No	No	No	85%
[17]	E	IR	TM	–	–	–	–	N/A
[18]	T	Visible	TM/TE	Yes**	No	No	No	5-20%
PRESENT	T	UV to EUV (≤18 PHz)	TM/TE	Yes***	Yes	Yes	Yes	82%

* Constant Complex Number.
** Oversimplified Model.
*** Expanded Via Inductive Reasoning.

and TE polarized input signals oriented in the Γ-M direction. Notably, for all cases shown, we observe blue-shifted and broadened Bragg resonances with reduced peaks as R increases. The latter is primarily due to increasing absorption by the absorbing medium (MWCNTs), deteriorating Bragg resonances as the R-value increases while keeping other geometrical parameters constant. It is also noteworthy that the blue-shifted and broadened Bragg reflectance spectra (photonic gaps) for MWCNT-PhCs with larger R/a are opposite to the photonic behavior observed in standard rod-based PhCs, which exhibit red-shifted and narrowed photonic gaps with increasing rod radii [23]. These differences are because the refractive index contrast for dielectric/air in conventional rod-based PhC changes in the opposite direction than that of the MWCNT/air, with Re $n_{TE(TM)} < 1$ (air) (Figure A.1), as R increases.

3- 5- Effect of ρ (r/R) on photonic responses

In subsection 3.4, we maintained a constant ratio of the inner to outer radii ($\rho = r/R$) of MWCNTs, significantly influencing the optical responses of MWCNT-PhC. To achieve a range of $0.1 \leq \rho \leq 0.3$ while keeping $N = 200$, $a = 25$ nm, and $R = 5$ nm fixed, we varied the inner radii and obtained Bragg reflectance spectra from the MWCNT-PhC illuminated by TM and TE polarized signals propagating in the Γ-X and Γ-M directions (Fig. 7). Our findings reveal slight redshifts and reduced reflectance peaks at the Bragg resonance as ρ increases. These results are consistent with

those of Fig. 6, albeit with a notable difference in the degree of redshifts. The decrease observed for each Bragg peak is due to the reduction in the density and the effectiveness of the scatterers as the inner radius increases. However, the practical Bragg's responses almost remain unchanged, knowing that inner radii of MWCNTs in the range of 0.75 to 1 nm are the most influential parameter in the fabricated samples [37].

Our findings suggest that the size of R is a crucial parameter in determining the photonic response of MWCNT-PhCs. These observations hold significant implications for the design and optimization of MWCNT-PhCs for various applications in EUV and soft X-ray devices, such as UV mirrors, lenses, and collimators. Further research is warranted to investigate the impact of other geometrical parameters on the photonic response of MWCNT-PhCs. Overall, our insights into the behavior of MWCNT-PhCs can facilitate the design and optimization of similar structures for practical applications [38].

Table 1 demonstrates where the present work stands as compared with previously published studies on MWCNT-PhCs [7-10, 15-18] concerning the type of study, whether experimental (E), theoretical (T), or both (E/T), the operating frequency range, polarization types, use of physical models for the dielectric function, the inclusion of MWCNT hollow core effect, applying the Drude-Lorentz model for a wide-range simulation, Kramers-Kronig (K-K) compatibility, and reflectance (R).
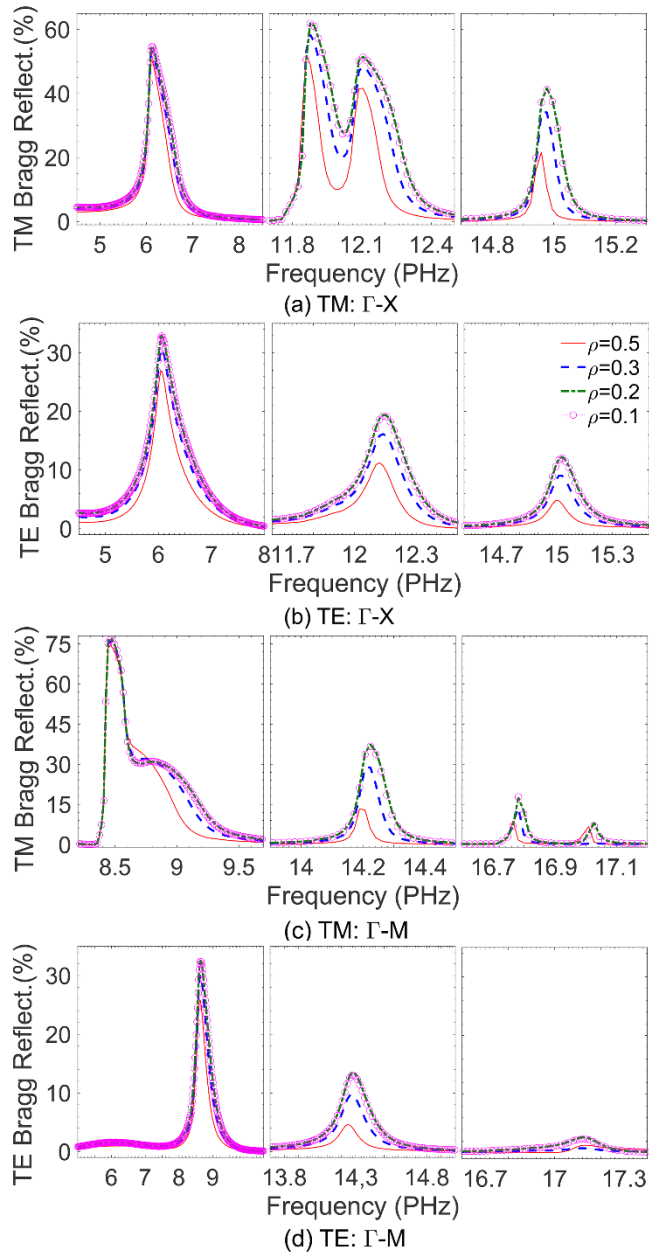
Fig. 7. Bragg reflectance spectra for various ρ and given values of N = 200, a =25 nm, and R = 5 nm, in response to combinations of polarization and lattice orientation (a) TM:Γ-X, (b) TE:Γ-X, (c) TM:Γ-M, and (d) TE:Γ-M.

4- Conclusion

The paper presents a comprehensive analysis of the photonic performances of β-aligned MWCNT ordered arrays, utilizing two experimentally and semi-empirically approved models for the dielectric function of an individual MWCNT in response to TM and TE incident waves. These models have been developed and fitted with the Drude-Lorentz model in earlier research and satisfy the Kramers-Kronig relations. The study employs the FDTD method to analyze the dependence of the photonic responses on the PhC geometrical parameters and incident signal orientation.

The results demonstrate the sound operation of the photonic structure up to extreme UV, which can be tuned over a frequency span of deep to EUV, with applications ranging from UV mirrors to UV lenses, and collimators. The paper highlights that wavelength windows down to 15 nm, which remained almost unexplored for a while in PhC-based photonics, are now more available, making it possible to be applied in EUV and soft X-ray devices and applications. Overall, the study contributes significantly to the field of photonic structures and offers promising avenues for future research in the area.

Acknowledgment

Author contributions

Y. Shamsollahi: Conceptualization, Data curation, Formal analysis, Investigation, Methodology, Writing the original draft; M. K. Moravvej-Farshi: Funding acquisition, Project administration, Resources, Supervision, Validation, Visualization, Writing - review & editing.

Declaration of interests

The authors declare that they have no known competing financial interests or personal relationships that could have appeared to influence the work reported in this paper.

References

[1] deHeer, Walt A., W. S. Bacsa, A. Châtelain, T. Gerfin, R. Humphrey-Baker, L. Forro, and D. Ugarte. 1995. 'Aligned Carbon Nanotube Films: Production and Optical and Electronic Properties', Science, https://doi.org/10.1126/science.268.5212.845.

[2] Lin, M. F., F. L. Shyu, and R. B. Chen. 2000. 'Optical properties of well-aligned multiwalled carbon nanotube bundles', Physical Review B, http://link.aps.org/doi/10.1103/PhysRevB.61.14114.

[3] Pan, Hui, Yuanping Feng, and Jianyi Lin. 2005. 'Ab initio study of electronic and optical properties of multiwall carbon nanotube structures made up of a single rolled-up graphite sheet', Physical Review B, http://link.aps.org/doi/10.1103/PhysRevB.72.085415.

[4] Liu, Xuchun, Jinhai Si, Baohe Chang, Gang Xu, Qiguang Yang, Zhengwei Pan, Sishen Xie, Peixian Ye, Junhua Fan, and Meixiang Wan. 1999. 'Third-order optical nonlinearity of the carbon nanotubes', Applied Physics Letters, https://doi.org/10.1063/1.123282.

[5] Maeda, A., S. Matsumoto, H. Kishida, T. Takenobu, Y. Iwasa, M. Shiraishi, M. Ata, and H. Okamoto. 2005. 'Large Optical Nonlinearity of Semiconducting Single-Walled Carbon Nanotubes under Resonant Excitations', Physical Review Letters, http://link.aps.org/doi/10.1103/PhysRevLett.94.047404.

[6] Misewich, J. A., R. Martel, Ph Avouris, J. C. Tsang, S. Heinze, and J. Tersoff. 2003. 'Electrically Induced Optical Emission from a Carbon Nanotube FET', Science, http://www.sciencemag.org/content/300/5620/783.abstract.

[7] Kempa, K., B. Kimball, J. Rybczynski, Z. P. Huang, P. F. Wu, D. Steeves, M. Sennett, M. Giersig, D. V. G. L. N. Rao, D. L. Carnahan, D. Z. Wang, J. Y. Lao, W. Z. Li, and Z. F. Ren. 2002. 'Photonic Crystals Based on Periodic Arrays of Aligned Carbon Nanotubes', Nano Letters, https://doi.org/10.1021/nl0258271.

[8] Lidorikis, Elefterios, and Andrea C. Ferrari. 2009. 'Photonics with Multiwall Carbon Nanotube Arrays', ACS Nano, https://doi.org/10.1021/nn900123a.

[9] Rybczynski, J., K. Kempa, Y. Wang, Z. F. Ren, J. B. Carlson, B. R. Kimball, and G. Benham. 2006. 'Visible light diffraction studies on periodically aligned arrays of carbon nanotubes: Experimental and theoretical comparison', Applied Physics Letters, https://doi.org/10.1063/1.2205165.

[10] Shamsollahi, Y., M. K. Moravvej-Farshi, and M. Ebnali-Heidari. 2013. 'Photonic Crystals Based on Periodic Arrays of MWCNTs: Modeling and Simulation', Lightwave Technology, Journal of, https://doi.org/10.1109/JLT.2013.2261952.

[11] Ren, Z. F., Z. P. Huang, J. W. Xu, J. H. Wang, P. Bush, M. P. Siegal, and P. N. Provencio. 1998. 'Synthesis of Large Arrays of Well-Aligned Carbon Nanotubes on Glass', Science, https://doi.org/10.1126/science.282.5391.1105.

[12] Chhowalla, M., K. B. K. Teo, C. Ducati, N. L. Rupesinghe, G. A. J. Amaratunga, A. C. Ferrari, D. Roy, J. Robertson, and W. I. Milne. 2001. 'Growth process conditions of vertically aligned carbon nanotubes using plasma enhanced chemical vapor deposition', Journal of Applied Physics, https://doi.org/10.1063/1.1410322.

[13] Teo, K. B. K., M. Chhowalla, G. A. J. Amaratunga, W. I. Milne, D. G. Hasko, G. Pirio, P. Legagneux, F. Wyczisk, and D. Pribat. 2001. 'Uniform patterned growth of carbon nanotubes without surface carbon', Applied Physics Letters, https://doi.org/10.1063/1.1400085.

[14] Lin, M. F. 2000. 'Optical spectra of single-wall carbon nanotube bundles', Physical Review B, http://link.aps.org/doi/10.1103/PhysRevB.62.13153.

[15] Butt, Haider, Qing Dai, Timothy D. Wilkinson, and Gehan A. J. Amaratunga. 2012. 'Negative index photonic crystal lenses based on carbon nanotube arrays', Photonics and Nanostructures - Fundamentals and Applications, https://doi.org/10.1016/j.photonics.2012.04.003.

[16] Butt, Haider, Qing Dai, Ranjith Rajesekharan, Timothy D. Wilkinson, and Gehan A. J. Amaratunga. 2011. 'Plasmonic Band Gaps and Waveguide Effects in Carbon Nanotube Arrays Based Metamaterials', ACS Nano, https://doi.org/10.1021/nn203363x.

[17] Wang, Y., X. Wang, J. Rybczynski, D. Z. Wang, K. Kempa, and Z. F. Ren. 2005. 'Triangular lattice of carbon nanotube arrays for negative index of refraction and subwavelength lensing effect', Applied Physics Letters, https://doi.org/10.1063/1.1900941.

[18] Bao, Hua, Xiulin Ruan, and Timothy S. Fisher. 2010. 'Optical properties of ordered vertical arrays of multi-walled carbon nanotubes from FDTD simulations', Opt. Express, http://www.opticsexpress.org/abstract.cfm?URI=oe-18-6-6347.

[19] Lü, Wengang, Jinming Dong, and Zhen-Ya Li. 2000. 'Optical properties of aligned carbon nanotube systems studied by the effective-medium approximation method', Physical Review B, http://link.aps.org/doi/10.1103/PhysRevB.63.033401.

[20] Henrard, L., and Lambin Ph. 1996. 'Calculation of the energy loss for an electron passing near giant fullerenes', Journal of Physics B: Atomic, Molecular and Optical Physics, http://stacks.iop.org/0953-4075/29/i=21/a=024.

[21] Wang, L., A. Tikhonov, and S. A. Asher. 2012. 'Silica Crystalline Colloidal Array Deep Ultraviolet Narrow-band Diffraction Devices', Appl. Spectrosc., vol. 66, p. 426, 2012.

[22] Corso, Alain J., and Maria G. Pelizzo. 2019. 'Extreme Ultraviolet Multilayer Nanostructures and Their Application to Solar Plasma Observations: A Review', Journal of Nanoscience and Nanotechnology, https://doi.org/10.1166/jnn.2019.16477.

[23] Joannopoulos, J.D. 2008. Photonic crystals: molding the flow of light (Princeton University Press).

[24] Spiller, Eberhard. 1990. "Soft-x-ray optics." In OSA Annual Meeting, TuB1. Optica Publishing Group.

[25] Golub, L., M. Herant, K. Kalata, I. Lovas, G. Nystrom, F. Pardo, E. Spiller, and J. Wilczynski. 1990. 'Sub-arcsecond observations of the solar X-ray corona', Nature, https://doi.org/10.1038/344842a0.

[26] Brown, C. M., U. Feldman, J. F. Seely, M. C. Richardson, H. Chen, J. H. Underwood, and A. Zigler. 1988. 'Imaging of laser-produced plasmas at 44 Å using a multilayer mirror', Optics Communications, https://

doi.org/10.1016/0030-4018(88)90183-6.

[27] Montcalm, C., P. A. Kearney, J. M. Slaughter, B. T. Sullivan, M. Chaker, H. Pépin, and C. M. Falco. 1996. 'Survey of Ti-, B-, and Y-based soft x-ray-extreme ultraviolet multilayer mirrors for the 2- to 12-nm wavelength region', Appl Opt, https://doi.org/10.1364/ao.35.005134.

[28] Li, Yuping, Ruonan Li, Huimin bian, Huijun Hu, Kai Zhang, and Peide Han. 2020. 'Photonic crystal films with high reflectance based on mesoporous silica in the extreme ultraviolet range', Optics Communications, https://doi.org/10.1016/j.optcom.2020.126110.

[29] Palik, E.D. 1991. Handbook of optical constants of solids II (Academic Press).

[30] Djurisic, Aleksandra B., and E. Herbert Li. 1999. 'Optical properties of graphite', Journal of Applied Physics, https://doi.org/10.1063/1.369370.

[31] Kuzmenko, A. B. 2005. 'Kramers–Kronig constrained variational analysis of optical spectra', Review of Scientific Instruments, https://doi.org/10.1063/1.1979470.

[32] Alexander Corletto, Joseph G. Shapter, 2007. 'Nanoscale Patterning of Carbon Nanotubes: Techniques, Applications, and Future', Nanotechnology, https://doi.org/10.1002/advs.202001778

[33] Stephen Y. Chou; Peter R. Krauss; Preston J. Renstrom, 1995. 'Imprint of Sub-25 nm Vias and Trenches in Polymers', Applied Physics Letters, https://doi.org/10.1063/1.114851

[34] M. J. Misner, 2003. 'Fabrication of Periodic Arrays of Metal Nanowires Using Interference Lithography and Electrodeposition', Nano Letters, 2003)

[35] Taft, E. A., and H. R. Philipp. 1965. 'Optical Properties of Graphite', Physical Review, http://link.aps.org/doi/10.1103/PhysRev.138.A197.

[36] Kuzmiak, V., A. A. Maradudin, and F. Pincemin. 1994. 'Photonic band structures of two-dimensional systems containing metallic components', Physical Review B, http://link.aps.org/doi/10.1103/PhysRevB.50.16835.

[37] García-Vidal, F. J., J. M. Pitarke, and J. B. Pendry. 1997. 'Effective Medium Theory of the Optical Properties of Aligned Carbon Nanotubes', Physical Review Letters, http://link.aps.org/doi/10.1103/PhysRevLett.78.4289.

[38] Wooten, F. 1972. Optical properties of solids (Academic Press).

Appendix

A TE polarized incident wave leads to the polarizability per length for an individual MWCNT, (tubular fullerene), as given by [20]:

$$\alpha_m^a = 4\pi\varepsilon_0 R^{2m} \frac{(\varepsilon_\parallel^2 \ell^2 - 1)(\rho^{2\ell m} - 1)}{(\varepsilon_\parallel \ell - 1)^2 \rho^{2\ell m} - (\varepsilon_\parallel \ell + 1)^2} \qquad (A.1)$$

where *m* is the order of the Bessel function and for a TE-polarized external field *m*=1 [20], *a* indicates the cylinder is anisotropic, $\rho = r / R$, with *r* and *R* being radii of the inner and outer shells of the MWCNT and $\ell \equiv (\varepsilon_\perp / \varepsilon_\parallel)^{1/2}$. To develop a model for $\varepsilon_{TE}(\omega)$ one must have a set of data for $\alpha_m(\omega)$ [10]. To obtain such data, we have used the collective experimental data for $\varepsilon_\parallel$ presented by [30] that satisfies the KK relation for the whole range of frequencies.

To develop our model, we have also considered a hypothetical isotropic cylinder with the same inner and outer radii as those of the assumed MWCNT. The polarizability of this hypothetical isotropic cylinder can be obtained by setting $\varepsilon_\perp = \varepsilon_\parallel = \varepsilon$ in Eq. (A1) [10]:

$$\alpha_m^i = 4\pi\varepsilon_0 R^{2m} (\varepsilon^2 - 1)(\rho^{2\ell m} - 1)/[(\varepsilon - 1)^2 \rho^{2\ell m} - (\varepsilon + 1)^2] \qquad (A.2)$$

where *i* indicates the isotropicity of the assumed hypothetical cylinder. Whenever this polarizability becomes equal to that of the anisotropic MWCNT (i.e., $\alpha_m^i = \alpha_m^a$) under the same TE incident wave, ε_{TE} of the assumed MWCNT will be equal to the dielectric function of the hypothetical isotropic cylinder; i.e., $\varepsilon_{TE}(\omega) = \varepsilon(\omega)$. Equating (A1) and (A2) leads us to a quadratic equation for ε_{TE} that is [10]:

$$A\varepsilon_{TE}^2 + B\varepsilon_{TE} + C = 0 \qquad (A.3a)$$

where,

$$A = (1 + \ell\varepsilon_\parallel) + (1 - \ell\varepsilon_\parallel)(\rho^{2m(\ell+1)} - \rho^{2\ell m} - \rho^{2m}) \qquad (A.3b)$$

$$B = \left(\ell^2 \varepsilon_\parallel^2 - 1\right)\left(\rho^{2m(\ell+1)} + \rho^{2\ell m} - \rho^{2m} - 1\right) \tag{A.3c}$$

$$C = \ell\varepsilon_\parallel(1 - \ell\varepsilon_\parallel)\left(\rho^{2m(\ell+1)} - \rho^{2\ell m} - \rho^{2m} + 1\right) \tag{A.3d}$$

Now, to perform our numerical simulations for PhCs consisting of an array of such MWCNTs, employing FDTD, we need to present these data in the form of the Drude-Lorentz formula:

$$\varepsilon_{TE}(\omega) = \varepsilon_\infty + \sum_{j=1}^{M} s_j^2 / \left(\omega_j^2 - \omega^2 - i\omega\gamma_j\right) \tag{A.4}$$

wherein ε_∞ is the relative permittivity as the frequency approaches infinity ($\omega \to \infty$) and ω_j, and γ_j are the oscillation frequencies and corresponding decay rates, respectively, and $s_j = \omega_p(f_j)^{1/2}$ in which ω_p is the plasma frequency and f_j represent the oscillators' strengths. Assuming $M=7$ and using the aforementioned parameters as fit parameters given in Table A.1 we have obtained the dotted and dashed lines in Fig. 1(b) in the paper.

Table A.1. Fit parameters used to obtain DL data presented by dotted and dashed lines in Fig. 1(b), using $\varepsilon_\infty = 0.925$.

J	$\hbar\omega_j$ (eV)	$\hbar\gamma_j$ (eV)	$\hbar s_j$ (eV)
1	0.368	4.917	1.064
2	5.016	2.152	5.347
3	10.058	1.870	3.332
4	14.357	2.392	10.765
5	16.741	5.047	8.160
6	22.451	13.282	13.417
7	26.869	1157.378	69.595

Note that the relation between plasma frequency ω_p of an individual MWCNT for a TE-wave incident, on the graphite's $\omega_{p,\perp} = 27$ eV and $\omega_{p,\parallel} = 19$ eV [30] is similar to the relation between the corresponding dielectric function ε_{TE} of the individual MWCNT and graphite's $\varepsilon_\parallel$ and $\varepsilon_\perp$, hence resulting in $\omega_{p,\,TE} \sim 23$ eV [10].

Finally, the complex refractive index for any given material can be written as $n = n_{Re} + i\,n_{Im}$. On the other hand, the relation between its real (n_{Re}) and imaginary (n_{Im}) parts with those of the permittivity, in general, is given by [35]:

$$\mathrm{Re}\, n = \left[\left(\sqrt{Re\varepsilon^2 + Im\varepsilon^2} + Re\varepsilon\right)/2\right]^{1/2} \tag{A.5a}$$

$$\mathrm{Im}\, n = \left[\left(\sqrt{Re\varepsilon^2 + Im\varepsilon^2} - Re\varepsilon\right)/2\right]^{1/2} \tag{A.5b}$$
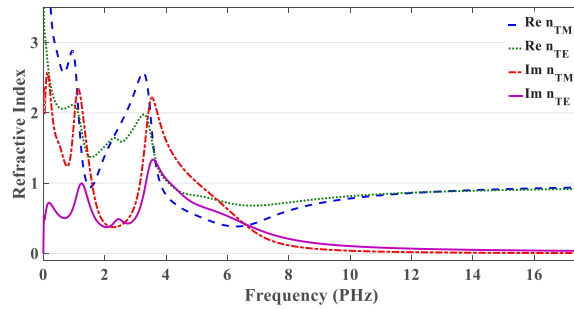

Fig. A.1. Real and imaginary parts of complex refractive indices for an individual MWCNT in response to TM and TE incident waves.

Substituting the modeled data for ε_{TM} and ε_{TE} as illustrated in Fig. 1(a) and (b) in Eq. (A5) one can obtain the real and imaginary parts of both n_{TM} and n_{TE}, as depicted in Fig. A.1. As observed from this figure, in the frequency range larger than 4.2 PHz, Re(n_{TM}) and Re(n_{TE}) are both less than unity. This implies that in any PhC made of an array of MWCNTs with Bragg response in this range of frequencies, the material (tubes) index is less than that of the surrounding environment (air), which is contrary to the situation of a PhC made of ordinary dielectric cylinders [23]. Hence, Bragg responses from MWCNT-PhCs are intended to function in this range of frequencies like air-hole PhCs based on usual dielectric platforms [23]. For instance, as the ratio *R/a* increases, one observes a blue-shifted and broadened photonic bandgap for TM incident waves of Fig. 6.